


Distinct roles for the Charcot–Marie–Tooth disease-causing endosomal regulators Mtmr5 and Mtmr13 in axon radial sorting and Schwann cell myelination

Anna E. Mammel^{1,2}, Katherine C. Delgado¹, Andrea L. Chin¹, Alec F. Condon^{1,3}, Jo Q. Hill⁴, Sue A. Aicher⁴, Yingming Wang⁵, Lev M. Fedorov⁵ and Fred L. Robinson^{1,6,*} 

¹The Jungers Center for Neurosciences Research, Department of Neurology, Oregon Health & Science University, Portland, OR 97239, USA

²Cell, Developmental & Cancer Biology Graduate Program, Department of Cell, Developmental and Cancer Biology, Oregon Health & Science University, Portland, OR, 97239, USA

³Neuroscience Graduate Program, Vollum Institute, Oregon Health & Science University Portland, OR, 97239, USA

⁴Department of Chemical Physiology and Biochemistry, Oregon Health & Science University, Portland, OR, 97239, USA

⁵OHSU Transgenic Mouse Models Shared Resource, Knight Cancer Institute, Oregon Health & Science University, Portland, OR, 97239, USA

⁶Vollum Institute, Oregon Health & Science University, Portland, OR, 97239, USA

*To whom correspondence should be addressed. Tel: +1 5032157457; Email: fred.robinson@providence.org

†Present address: Earle A. Chiles Research Institute, A Division of Providence Cancer Institute, 4805 NE Glisan Street, Suite 2N13, Portland, OR 97213, USA.

Abstract

The form of Charcot–Marie–Tooth type 4B (CMT4B) disease caused by mutations in myotubularin-related 5 (MTMR5; also called SET binding factor 1, SBF1) shows a spectrum of axonal and demyelinating nerve phenotypes. This contrasts with the CMT4B subtypes caused by MTMR2 or MTMR13 (SBF2) mutations, which are characterized by myelin outfoldings and classic demyelination. Thus, it is unclear whether MTMR5 plays an analogous or distinct role from that of its homolog, MTMR13, in the peripheral nervous system (PNS). MTMR5 and MTMR13 are pseudophosphatases predicted to regulate endosomal trafficking by activating Rab GTPases and binding to the phosphoinositide 3-phosphatase MTMR2. In the mouse PNS, Mtmr2 was required to maintain wild-type levels of Mtmr5 and Mtmr13, suggesting that these factors function in discrete protein complexes. Genetic elimination of both Mtmr5 and Mtmr13 in mice led to perinatal lethality, indicating that the two proteins have partially redundant functions during embryogenesis. Loss of Mtmr5 in mice did not cause CMT4B-like myelin outfoldings. However, adult *Mtmr5*^{-/-} mouse nerves contained fewer myelinated axons than control nerves, likely as a result of axon radial sorting defects. Consistently, Mtmr5 levels were highest during axon radial sorting and fell sharply after postnatal day seven. Our findings suggest that Mtmr5 and Mtmr13 ensure proper axon radial sorting and Schwann cell myelination, respectively, perhaps through their direct interactions with Mtmr2. This study enhances our understanding of the non-redundant roles of the endosomal regulators MTMR5 and MTMR13 during normal peripheral nerve development and disease.

Introduction

During the development of the peripheral nervous system (PNS), Schwann cells associate with bundles of mixed diameter axons. In a process known as radial sorting, Schwann cells segregate large diameter axons (>1 μm) from smaller axons, which remain in bundles (1,2). Once sorted into 1:1 associations with Schwann cells, large caliber axons are wrapped in a specialized, multilayer membrane sheath called myelin (3). Myelin facilitates rapid, saltatory nerve impulse conduction by clustering sodium channels at nodes of Ranvier and by reducing axonal capacitance (4). Small caliber axons (<1 μm) remain unmyelinated and are supported by Schwann cells in Remak bundles (2). Both myelinating and Remak Schwann cells provide metabolic support to maintain axon integrity (3,5–8). Both radial sorting and subsequent myelination require coordinated

cytoskeleton reorganization, and receptor signaling from the adaxonal and abaxonal Schwann cell surfaces (1,3). The precise control of downstream signaling is thought to be mediated in part by receptor trafficking through the endo-lysosomal pathway (9–11).

Genomic studies have strongly suggested a link between abnormal endosomal trafficking and demyelinating Charcot–Marie–Tooth (CMT) disease (12). CMT is the most common inherited neurological disorder, affecting 1 in 2500 people (13). Axonal and demyelinating forms of CMT are defined clinically, and are typically caused by mutations that initially affect axons and Schwann cells, respectively (14). CMT type 4 (CMT4) is characterized by autosomal recessive inheritance and demyelination (15). Nearly half of the human proteins that, when mutated, cause CMT4 are proposed to regulate membrane trafficking through endo-lysosomal compartments. These

proteins include dynamin 2 (*DNM2*), factor-induced gene 4 (*FIG4*), FGD1-related F-actin-binding protein (*FRABIN*), lipopolysaccharide-induced tumor necrosis factor- α factor (*LITAF*), SH3 domain and tetratricopeptide repeats 2 (*SH3TC2*), myotubularin-related 2 (*MTMR2*), *MTMR5* and *MTMR13* (12). Several of these proteins, including *FIG4*, *FRABIN*, *MTMR2*, *MTMR5* and *MTMR13*, control endo-lysosomal trafficking by enzymatically modifying or binding to phosphoinositides (PIs). Despite the generally broad expression of these genes in mammalian tissues, mutations therein primarily impact the PNS, suggesting that myelinating Schwann cells are highly sensitive to disruptions in endo-lysosomal membrane trafficking (12,16).

CMT4B results from mutations in *MTMR2*, *MTMR5* (also known as SET binding factor 1; *SBF1*) or *MTMR13* [*SBF2*; Fig. 1; (17–19)]. Myotubularins are a large family of phosphoinositide 3-phosphatases that regulate membrane trafficking through endosomes and lysosomes (20). This family of proteins includes both catalytically active and inactive phosphatase enzymes. *MTMR2* contains an active phosphatase domain, whereas *MTMR5* and *MTMR13* contain catalytically inactive phosphatase domains (20,21). *MTMR5* and *MTMR13* share 59% protein identity and possess the same unique set of protein domains, including a DENN domain that activates Rab GTPases, and a coiled-coil motif that facilitates association with *MTMR2* (Fig. 1). *MTMR2* and *MTMR13* are thought to function as a membrane-associated complex that regulates PI levels and drives Rab GTPase activation to influence the trafficking of key Schwann cell receptors through endosomes (22–25). However, it remains unclear if *MTMR5*, which also binds avidly to *MTMR2* (26), plays an analogous role to *MTMR13* in the PNS.

The human nerve pathology associated with homozygous mutations in *MTMR2* or *MTMR13* is well characterized and features distinctive myelin outfoldings thought to arise from excessive longitudinal myelin growth, as well as demyelination, and severe, presumably secondary, axon loss (17,19). In contrast, *MTMR5*-associated neuropathies show broader clinical presentations, which include myelin outfoldings, axon loss, thin myelin and bands of Bungner (18,27,28). To date, five families have been identified with CMT-causing mutations in *MTMR5*; a majority of these patients bear missense mutations within or near the DENN-domain [Fig. 1; (18,27–30)]. Thus, it remains unclear whether *MTMR5* loss-of-function causes myelin outfoldings analogous to those observed in the nerves of CMT4B1 (*MTMR2*) and CMT4B2 (*MTMR13*) patients.

To elucidate the role of *Mtmr5* in the PNS, we generated an *Mtmr5* knockout mouse model using CRISPR-Cas9 gene editing, and subsequently assessed the pathological consequences of the loss of *Mtmr5* on peripheral nerves. We used biochemical approaches to determine how the three CMT-causing *Mtmr* proteins physically interact, and inferred how these interactions may relate to the observed nerve phenotypes. Our study indicates that

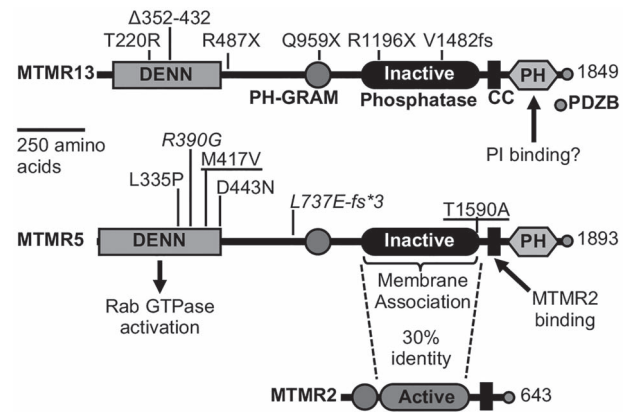


Figure 1. CMT-causing mutations in the *MTMR13* and *MTMR5* proteins. All mutations are recessive, consistent with a loss-of-function mechanism of pathogenesis. Functions attributed to specific domains of *MTMR13/5* are indicated. *MTMR5* mutations M417V-T1590V and R390G-L737E-fs*3 are shown underlined and in italics, respectively, to indicate compound heterozygosity in the corresponding patients. The *MTMR13* mutation T220R was identified in a patient with Griscelli syndrome. *MTMR5* shares 59% identity with *MTMR13*. The inactive phosphatase domains of *MTMR5* and *MTMR13* are ~30% identical to the PI 3-phosphatase domain of *MTMR2*. Abbreviations: PH, pleckstrin homology; DENN, differentially expressed in neoplastic versus normal; GRAM, Glucosyltransferases, Rab Activators, Myotubularins; PDZB, PDZ domain Binding; CC, Coiled-Coil; PI, Phosphoinositide.

the homologous proteins, *Mtmr5* and *Mtmr13*, require *Mtmr2* to maintain their wild-type protein level in the PNS, but play distinct roles during axon radial sorting and myelination.

Results

A novel deletion allele of *Mtmr5*

Initial characterization of an *Mtmr5* deletion allele in mice was described prior to the discovery that mutations in human *MTMR5* cause CMT4B3 disease (31). The previously described *Mtmr5* deletion causes male infertility, but whether these mice develop peripheral nerve defects was not examined (31). We attempted to reestablish this mouse line using intracytoplasmic sperm injection, but were unsuccessful. Therefore, an *Mtmr5* deletion allele was generated using CRISPR-Cas9 mutagenesis and subsequently assessed for nerve defects. To target *Mtmr5*, guide RNAs (gRNAs) were designed to target exon 1 and exon 25 (Fig. 2A). Founder mice were screened for mutations in exon 1 and/or large deletions that removed the sequences between exon 1 and exon 25. A founder mouse was determined to be mosaic for two distinct fusions of exon 1 and exon 25 (mutations 1 and 2; Fig. 2A). Only mutation 2 was passed to progeny mice (Fig. 2B). This novel *Mtmr5* mutation is predicted to yield a frameshift that leads to a premature stop codon in exon 25; translation would result in a non-functional six amino acid peptide (Fig. 2A; Supplementary Material, Fig. S1).

Consistent with the predicted gene disruption, the full-length 208 kDa *Mtmr5* protein was undetectable in sciatic nerve and brain extracts from adult *Mtmr5*^{-/-} mice (Fig. 2C and D). However, a truncated *Mtmr5*

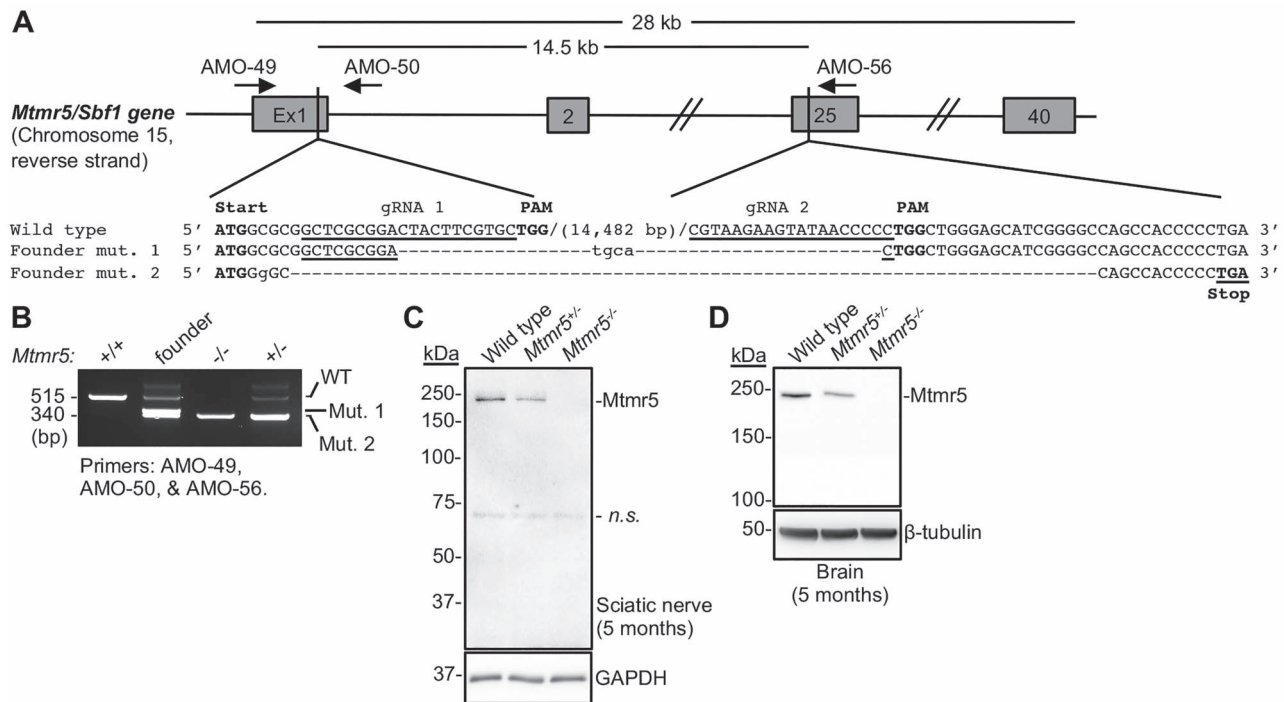


Figure 2. CRISPR/Cas9-mediated disruption of *Mtmr5*. (A) A CRISPR-Cas9-mediated 14 kb deletion between exon 1 and exon 25 of *Mtmr5/Sbf1*. The following features are indicated: gRNA target sequences (underlined), translation start site (**bold**), PAM sequences (**bold**), premature stop codon (**bold and underlined**) and additional mutations (*lower case*). The CRISPR-Cas9-modified founder mouse was mosaic for two deletions, termed mutations 1 and 2 (mut. 1, mut. 2). The genomic locations and orientations of the genotyping primers AMO-49, AMO-50 and AMO-56 are indicated. (B) Genotyping of a wild-type mouse produces a 515 bp PCR fragment. The F1 generation and all subsequent intercrosses contained mutation 2 deletion exclusively. (C, D) Immunoblot analyses of *Mtmr5* protein levels from sciatic nerve and brain extracts from 5-month-old wild-type, *Mtmr5*^{+/-} and *Mtmr5*^{-/-} mice using a C-terminal *Mtmr5* antibody. Each sciatic nerve extract was prepared by pooling two nerves. Representative data from one of three independent experiments are shown. The protein loading controls were GAPDH and β -tubulin.

Table 1. Male sterility in the absence of *Mtmr5*

Breeding pair			
M x F	Pairs mated (no.)	Litters (no.)	Litter size
+/+ +/-	3	3	6 ± 2
+/- +/-	9	9	6 ± 1
+/- -/-	3	3	3 ± 1
-/- +/+	6	0	0

protein of 84.8 kDa was detected at a low level in brain extracts from postnatal day 7 (P7) *Mtmr5*^{-/-} and *Mtmr5*^{+/-} mice (Supplementary Material, Fig. S2). We predict that translational initiation at an ATG codon in exon 26 leads to low-level expression of this truncated *Mtmr5* protein, at least in neonatal mouse brains. The described, N-terminally truncated *Mtmr5* protein was not detected in adult brain or sciatic nerve extracts (Supplementary Material, Fig. S2). When expressed, the truncated protein may be non-functional, as it lacks both the DENN and PH-GRAM domains (Fig. 1).

Mtmr5^{-/-} mice were viable and observed at the frequency predicted by Mendelian genetics. Homozygous mutants of both sexes were ~30% smaller than wild-type and *Mtmr5*^{+/-} controls (Supplementary Material, Fig. S3). This weight difference was observed at weaning and continued throughout the life of the animal. Overt motor or gait deficiencies were not observed in *Mtmr5*^{-/-}

mice examined at P38 and 17 months (*data not shown*). *Mtmr5*^{-/-} males were sterile (Table 1), consistent with previous observations made using a distinct deletion allele (31). The absence of *Mtmr5* protein expression, and the sterility of *Mtmr5*^{-/-} males strongly suggests that the mutation described here is a null or strongly *hypermorphic* allele.

Biochemical relationships amongst CMT-linked myotubularins

MTMR5 and MTMR13 are each known to bind avidly to MTMR2 in a manner that requires coiled-coil sequences (26,32). However, it is unclear whether the pseudophosphatases also interact with each other. To test their physical associations, we overexpressed epitope-tagged MTMR5 with MTMR13 and/or MTMR2 in HEK293 cells. MTMR5 and MTMR13 were found to associate in a manner that does not require coiled-coil motifs (Fig. 3A and B). In addition, an immunoprecipitation experiment using brain extracts suggested that *Mtmr5* and *Mtmr13* may form a complex that does not require the presence of *Mtmr2*. The co-expression of MTMR5 and MTMR13 did not enhance either protein's abundance (Fig. 3A and B). In contrast, co-expression of MTMR2 greatly increased the levels of both MTMR5 and MTMR13 (Fig. 3A and B). These data suggest that MTMR5 and MTMR13 may associate in manner that does not equate

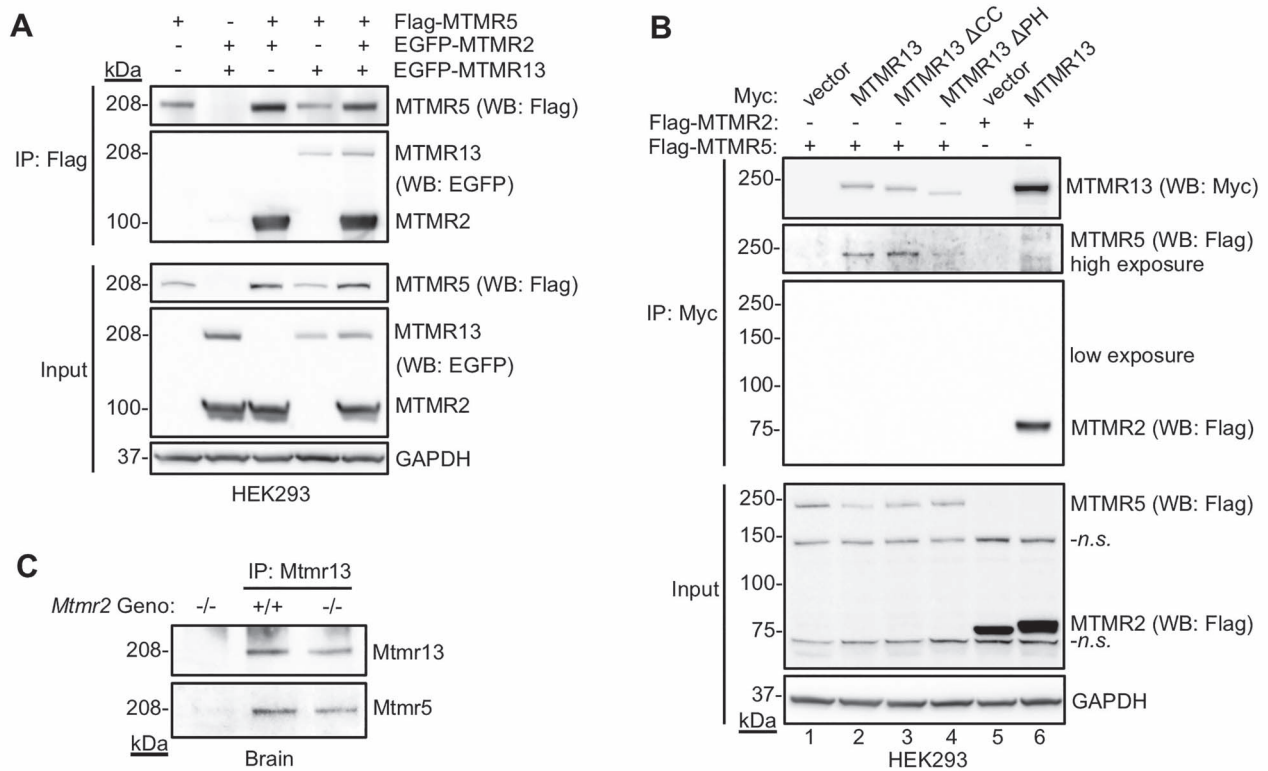


Figure 3. Physical associations between CMT-linked myotubularin proteins. **(A)** HEK293 cells were transfected with vectors expressing the indicated proteins. After 48 h, cell lysates were prepared and analyzed by FLAG immunoprecipitation (IP), SDS-PAGE and western blotting (WB). Co-expression of EGFP-MTMR2 increased the amount of FLAG-MTMR5 protein in the lysate and IP. Representative images from one of two experiments are presented. **(B)** HEK293 cells were transfected with constructs encoding FLAG or c-Myc epitope-tagged versions of the indicated myotubularin proteins. The association between FLAG-MTMR5 and myc-MTMR13 did not require the coiled-coil (CC) motif or the C-terminal pleckstrin homology (PH) domain of MTMR13. Co-expression of FLAG-MTMR2, but not FLAG-MTMR5 increased the recovery of immunoprecipitated myc-MTMR13 (compare lanes 2 and 6). Representative data from one of two independent experiments are shown. Non-specific (*n.s.*) cross-reactions of the anti-FLAG antibody with proteins present in cell lysates are indicated. **(C)** Coimmunoprecipitation of endogenous Mtmr13 and Mtmr5 from wild-type and *Mtmr2*^{-/-} mouse brains. The association between Mtmr5 and Mtmr13 was not altered by the absence of Mtmr2. The antibody used to detect Mtmr13 in the upper panel of Fig. 3C, has not been directly shown to lack all cross-reactivity with Mtmr5. Therefore, we cannot exclude the possibility that the protein band detected in the lower panel of Fig. 3C might in reality be Mtmr13. The data from a single experiment are shown.

to their association with MTMR2. The possibility that all three proteins may reside in the same protein complex cannot be excluded. Indeed, the precise aggregation state of MTMR2, MTMR5 and MTMR13 may be dictated by the relative abundance of the three proteins, rather than strictly by their biochemical affinities for each other.

We previously demonstrated that Mtmr2 and Mtmr13 require each other to maintain wild-type protein levels in mouse sciatic nerves (22). To determine if Mtmr2 and/or Mtmr13 proteins were required to regulate Mtmr5 levels, we examined mutant mouse brain and sciatic nerve lysates. Both Mtmr5 and Mtmr13 protein levels were significantly reduced in *Mtmr2*^{-/-} nerves (Fig. 4A and B). However, the requirement of Mtmr2 to maintain Mtmr5 at wild-type levels was not reciprocal; *Mtmr5*^{-/-} sciatic nerve lysates had comparable Mtmr2 levels with wild-type nerves (Fig. 4D and E). Mtmr13 loss had no impact on Mtmr5 levels in mouse brain or sciatic nerves, demonstrating that these pseudophosphatases do not require one another to maintain wild-type protein levels (Fig. 4A and C).

The stabilization of Mtmr5/13 by Mtmr2 was unique to the PNS; loss of Mtmr2 had no impact on the levels of Mtmr5 or Mtmr13 in brain extracts (Fig. 4C). In addition, loss of both Mtmr5 and Mtmr13 in *Mtmr5*^{-/-}; *Mtmr13*^{-/-} mouse embryonic fibroblasts (MEFs) did not impact Mtmr2 abundance (Fig. 4F and G). In summary, these data demonstrate that Mtmr2 is needed for wild-type levels of both Mtmr5 and Mtmr13 protein abundance, specifically in the PNS, where CMT disease manifests.

Reduced sciatic nerve axons and normal myelination in the absence of Mtmr5

In mice, the nerve pathology caused by the loss of Mtmr13 is well-characterized (33,34). In contrast, the mouse nerve pathology associated with the loss of Mtmr5 is undefined. Loss-of-function mutations in *MTMR13/Mtmr13* cause distinct Schwann cell myelin abnormalities known as myelin outfoldings in both CMT patients and mouse models (33–35). The role of MTMR5 in the PNS remains unclear; significantly different

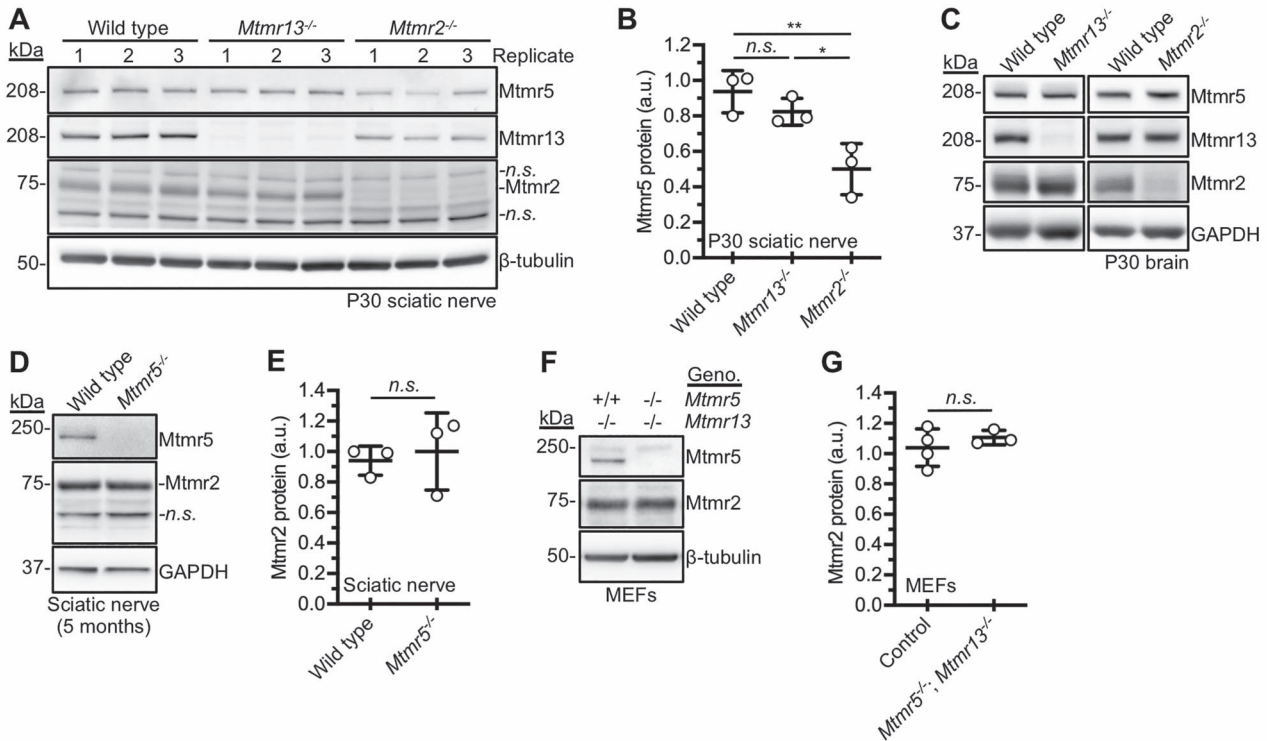


Figure 4. Relationships amongst CMT-linked myotubularin proteins assessed *in vivo*. (A) Sciatic nerve lysates were prepared from wild-type, *Mtmr13*^{-/-} and *Mtmr2*^{-/-} P30 mice. Pools 1, 2 and 3 denote independent (replicate) pools of nerves of the same genotype (4 nerves per lysate). Non-specific (n.s.) bands are indicated in *Mtmr2* blots. (B) Relative quantification of *Mtmr5* protein levels: wild-type 0.937 ± 0.115 , *Mtmr13*^{-/-} 0.825 ± 0.072 , *Mtmr2*^{-/-} 0.499 ± 0.147 (arbitrary units, a.u.; mean \pm SD; one-way ANOVA with post-hoc Tukey test; * $P < 0.05$; ** $P < 0.01$; n.s., not significant; $n = 3$ for each genotype). (C) Protein extracts from wild-type, *Mtmr13*^{-/-} and *Mtmr2*^{-/-} P30 brain lysates showed no significant differences in *Mtmr5* protein levels. Representative data from one of three independent experiments are shown. (D) Sciatic nerve lysates prepared from wild-type and *Mtmr5*^{-/-} animals at age 5 months (2 nerves per lysate) were analyzed by immunoblotting. (E) Quantitation of (D), *Mtmr2* protein: 0.937 ± 0.096 for wild-type versus 1.003 ± 0.253 for *Mtmr5*^{-/-} nerves ($P = 0.697$; $n = 3$ for each genotype; two-sample Student's *t*-tests; n.s., not significant). (F) Protein extracts from control (*Mtmr5*^{+/+}; *Mtmr13*^{-/-}) and *Mtmr5*^{-/-}; *Mtmr13*^{-/-} MEF cultures were immunoblotted for *Mtmr2*. (G) Quantitation of F. Significant differences in *Mtmr2* protein levels were not observed. *Mtmr2* protein: 1.040 ± 0.122 for controls (*Mtmr5*^{+/+}; *Mtmr13*^{-/-} or *Mtmr5*^{+/-}; *Mtmr13*^{-/-}) versus 1.104 ± 0.048 for *Mtmr5*^{-/-}; *Mtmr13*^{-/-}, respectively (mean \pm SD; $P = 0.258$; $n = 3-4$ per genotype; two-sample Student's *t*-tests; n.s., not significant).

pathology has been described in patient nerve biopsies (18,27,28). Through examination of *Mtmr5*^{-/-} mouse nerves, we sought to determine whether *Mtmr5* has a distinct or analogous role to that of *Mtmr13* in the PNS. At 3 months, the morphology of *Mtmr5*^{-/-} sciatic nerves appeared grossly normal (Fig. 5A–D). Loss of *Mtmr5* did not cause CMT4B-like myelin outfoldings, indicating a pathology distinct from that caused by the loss of *Mtmr13* (Fig. 5C–E). The absence of *Mtmr5* did not alter myelin thickness; g-ratios were not significantly different between *Mtmr5*^{-/-} and wild-type fibers (Fig. 5F). However, *Mtmr5*^{-/-} mice had significantly fewer total myelinated axons in sciatic nerves than wild-type controls (Fig. 5G). The absence of *Mtmr5* did not alter the diameter of myelinated axons, a feature of several mouse models of axonal CMT [Fig. 5H; (36,37)]. These data demonstrate that *Mtmr5*-deficiency causes nerve pathology distinct from that caused by the absence of *Mtmr13*. Thus, despite sharing a common binding partner (*Mtmr2*), and possessing similar protein structures, the two pseudophosphatases play distinct roles in the murine PNS.

Axonal sorting defects in the absence of *Mtmr5*

Incomplete radial sorting by immature Schwann cells can lead to the abnormal retention of large caliber axons in bundles, thereby reducing the total number of myelinated axon fibers in nerves (38,39). To determine whether the absence of *Mtmr5* caused abnormal Remak bundle development, we examined axon bundles in the sciatic nerve using EM. Wild type and *Mtmr5*^{-/-} sciatic nerves were characterized by determining the total number of axons per bundle, the proportion of bundled axons whose diameter exceeded $1 \mu\text{m}$, and whether bundled axons were incompletely enclosed by Schwann cell processes.

In *Mtmr5*^{-/-} nerves examined at 3 months, we observed a significant increase in the proportion of bundled axons that had a diameter of $>1 \mu\text{m}$ (Fig. 6A–C), indicating delayed or arrested sorting of some large axons from bundles. We also observed a significant increase in unmyelinated axons that were in 1:1 relationships with Schwann cells, although most such axons were smaller than $1 \mu\text{m}$ in diameter (Fig. 6D and I). The number of axons per bundle did not differ markedly

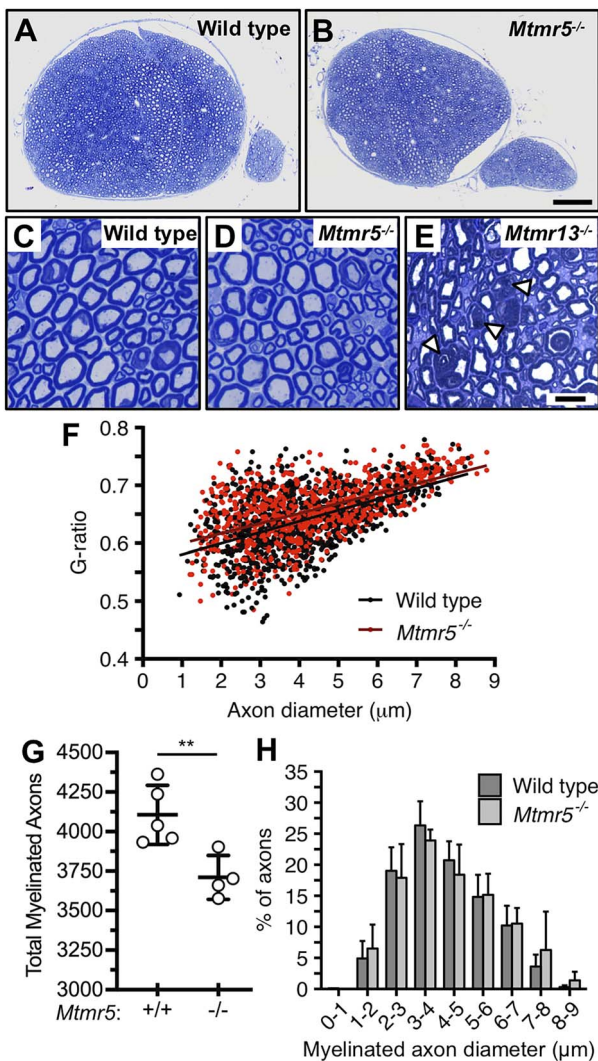


Figure 5. Sciatic nerve morphology in the absence of *Mtmr5*. (A, B) Comparable sciatic nerve cross-sections from wild-type and *Mtmr5*^{-/-} mice are shown (3 months of age). Scale bar: 100 μ m. (C, D) Toluidine blue-stained mid-sciatic nerve myelin appeared normal in *Mtmr5*^{-/-} mice; CMT4B-like myelin outfoldings were not observed. Scale bar: 10 μ m. (E) A comparable image of an *Mtmr13*^{-/-} mid-sciatic nerve stained with toluidine blue. Arrowheads indicate myelin outfoldings. (F) G-ratio analysis of myelin thickness in wild-type and *Mtmr5*^{-/-} nerves (best-fit line; $N = 4$ –5 mice; 200 myelinated axons per mouse). (G) The total number of myelinated axons in sciatic nerves of *Mtmr5*^{-/-} mice was significantly reduced at 3 months of age (mean \pm SD; ** $P < 0.01$; two-sample Student's t -test; $n = 4$ –5 mice per genotype). (H) Similar myelinated axon size distribution between wild-type and *Mtmr5*^{-/-} sciatic nerves (Two-sample Kolmogorov–Smirnov test; $P = 0.16$; wild-type, $N = 5$ mice, $n = 999$ axons; *Mtmr5*^{-/-}, $N = 4$ mice, $n = 799$ axons).

between wild type and *Mtmr5*^{-/-} nerves (Fig. 6D). However, a significant decrease in the percentage of bundles containing between 11 and 20 axons was observed in mutant nerves (Fig. 6D). Finally, bundled axons of *Mtmr5*^{-/-} nerves were significantly more likely to be incompletely enwrapped by Schwann cell processes, as evidenced by direct contact of axons with basal laminae (Fig. 6E–G). In aggregate, our findings indicate that *Mtmr5* positively regulates late-stage radial sorting of large caliber axons. We propose that, after the completion of radial sorting, *Mtmr5* is dispensable for subsequent

myelination, an assertion consistent with the normal myelin thickness and absence of CMT4B-like myelin outfoldings in *Mtmr5*^{-/-} nerves.

Loss of both *Mtmr5* and *Mtmr13* is lethal in mice

Mtmr5 and *Mtmr13* share 59% protein identity and are the only two proteins in the genome that share their unique set of protein domains [Fig. 1; (40)]. To assess whether these proteins might have partially redundant functions, we generated *Mtmr5*^{-/-}; *Mtmr13*^{-/-} double knockout (dKO) mice. dKO animals were non-viable, dying during late gestation or within a few hours of birth (Fig. 7). *Mtmr5*^{-/-}; *Mtmr13*^{-/-} embryos were observed at the expected Mendelian frequencies at embryonic (E) days 13–15, but were smaller than littermate controls; overt morphological defects were not apparent (Fig. 7, Supplementary Material, Fig. S4, and data not shown). In summary, the absence of both *Mtmr5* and *Mtmr13* leads to physiological deficits that preclude postnatal survival.

Mtmr5 and *Mtmr13* have critical roles in the PNS, and both are proposed to activate the early endosomal GTPase Rab21, a regulator of neurite growth and axon guidance (41,42). Accordingly, we assessed whether the combined loss of both proteins might alter axon guidance and/or peripheral nerve development during embryogenesis. We found that nerve branches in dKO mouse pinna, a region where axon guidance is well defined, appeared morphologically similar to those of controls (Supplementary Material, Fig. S4). Thus, a strict requirement for *Mtmr5* or *Mtmr13* for axon guidance appears unlikely.

Myotubularin expression in peripheral nerves and Schwann cells

We considered whether the phenotypic differences between *Mtmr5*^{-/-} and *Mtmr13*^{-/-} mice might correlate with the expression levels of the two proteins during PNS development. *Mtmr2*, *Mtmr5* and *Mtmr13* protein levels in sciatic nerves were therefore evaluated at distinct time points during mouse development (Fig. 8A–D). The levels of all three *Mtmr* proteins peaked at P7, the mid-way point of initial myelination (P0–P14; Fig. 8A–D). *Mtmr5* levels were significantly reduced by P21, although the protein remained detectable in adult nerves (Fig. 8A and B). *Mtmr13* and *Mtmr2* levels also decreased after P7, though less precipitously than *Mtmr5* levels (Fig. 8A–D). Thus, *Mtmr5* levels were highest during late stage radial sorting (E17–P10), consistent with our morphological findings indicating a role for the protein in this process. The sharp decrease in *Mtmr5* levels after P7 might indicate a relatively limited role for the protein in adult sciatic nerves.

We also evaluated the mRNA levels of all 14 myotubularin family members in adult mouse Schwann cells by analyzing a publicly available RNA-Seq dataset (43). This analysis indicated that *Mtmr2* and *Mtmr13* are expressed at significantly higher levels than nearly all other *Mtmr*

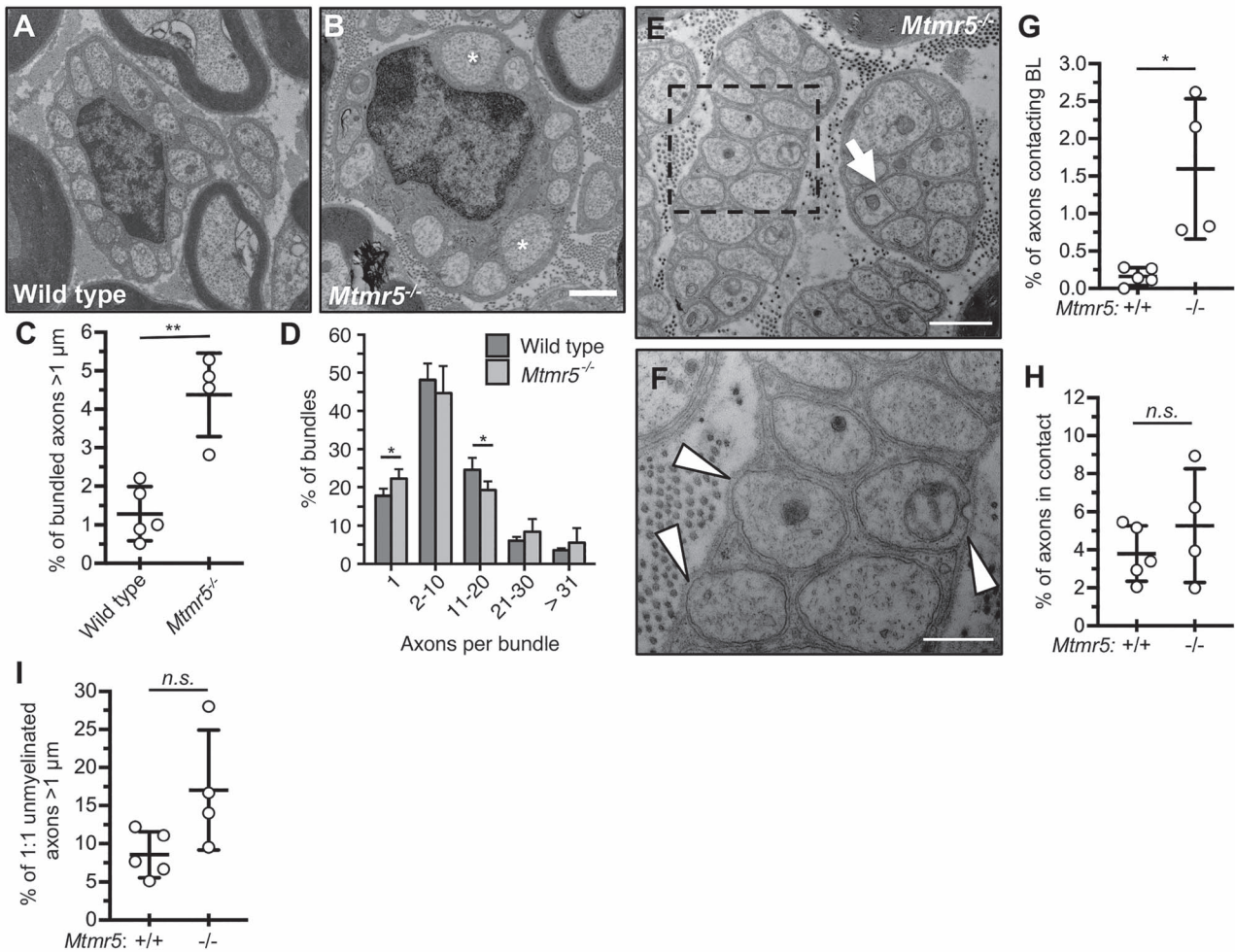


Figure 6. The absence of *Mtmr5* alters axon radial sorting and ensheathment. (A, B) EM images of representative axon bundles in sciatic nerves of wild-type and *Mtmr5*^{-/-} mice at 3 months. Asterisks indicate axons > 1 μm in diameter. Scale bar: 1 μm. (C) The percentage of bundled axons > 1 μm in diameter was significantly increased in *Mtmr5*^{-/-} sciatic nerves at 3 months (1.29 ± 0.70% for wild-type vs. 4.37 ± 1.09% for *Mtmr5*^{-/-}, respectively; n = 4–5 mice per genotype). (D) Number of axons per bundle expressed as a percentage. Categories are distinguished by the number of ensheathed axons. (E) EM of two bundles from a transverse *Mtmr5*^{-/-} sciatic nerve section. The arrow indicates an area without Schwann cell cytoplasm between axons. Scale bar: 1 μm. (F) Higher magnification image of the section boxed in image (E). Arrowheads identify points of direct contact between the basal lamina (BL) and axons. Scale bar: 500 nm. (G, H) Axons lacking full Schwann cell ensheathment were counted and expressed as a percentage of the total bundled axons per mouse. (G) Quantification of the percentage of axons abnormally contacting the Schwann cell BL. (H) Quantification of the percentage of axons in direct contact with another axon. (I) Quantification of the percentage of unmyelinated axons, in 1:1 relationships with Schwann cells (D), that were of > 1 μm in diameter (P = 0.0595). Data are mean ± SD; Student's t-test; *P ≤ 0.05; **P ≤ 0.01; n = 5 wild-type and n = 4 *Mtmr5*^{-/-} mice; n.s., not significant).

mRNAs in the Schwann cells of adult nerves (Fig. 8E). In contrast, *Mtmr5* mRNA was present at low levels in adult Schwann cells, consistent with the decreased *Mtmr5* protein that we observed in sciatic nerves examined after P7 (Fig. 8A, B and E). The observed temporal and cell type-specific differences in the expression of *Mtmr5* and *Mtmr13* correlate with the distinct PNS phenotypes of *Mtmr5*^{-/-} and *Mtmr13*^{-/-} mice.

Discussion

Mtmr5-deficient mice as a model CMT disease

Loss of *Mtmr5* in mice caused a ~10% reduction in the number of myelinated axons in the sciatic nerve due to radial sorting defects. Several patient families with loss-of-function mutations in *MTMR5* show moderate depletion of myelinated axons without defects in

myelin structure, suggesting primary axonal neuropathy (28,29). Given the findings presented here, we propose that abnormal axon radial sorting be considered as a potential primary defect in CMT associated with *MTMR5* loss-of-function. The effects of *MTMR5* loss-of-function may be exacerbated in humans relative to mice, potentially explaining the greater reductions in myelinated axon numbers observed in patients (28,29). Although the precise cause of this feature is unclear, several mouse models of axonal CMT have shown phenotypes milder than their corresponding human conditions (36,44–48). Incomplete radial sorting can be caused by defects in both axons and Schwann cells (1,49). Accordingly, future studies employing conditional *Mtmr5* knockout alleles will be needed to determine if *Mtmr5*'s role is restricted to axons or Schwann cells.

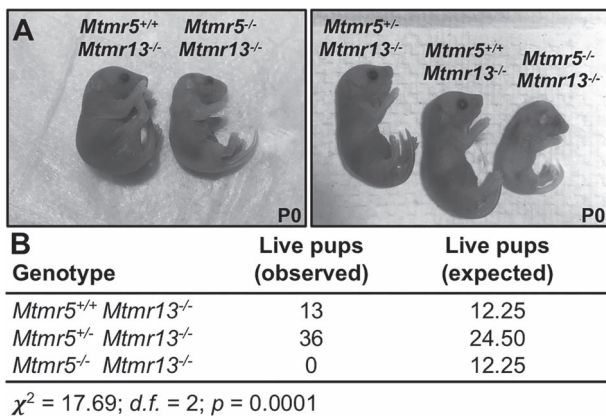


Figure 7. *Mtmr5*–*Mtmr13* double-knockout mice are not viable beyond birth. (A) Images of *Mtmr5*^{+/+}; *Mtmr13*^{-/-}; *Mtmr5*^{-/-}; *Mtmr13*^{-/-} mice found dead at P0, alongside littermate controls. (B) *Mtmr5*^{-/-}; *Mtmr13*^{-/-} dKO animals were not represented at the expected ratios (Chi-squared (χ^2) 17.69; *P* = 0.0001; *n* = 49 total live pups).

In the *Mtmr5*^{-/-} PNS, myelin was of normal thickness and structure, and notably lacked the distinctive myelin outfoldings caused by the absence of *Mtmr2* or *Mtmr13*. Nerve biopsies from a family of CMT patients with compound heterozygous mutations in *MTMR5* (M417V and T1590A) showed CMT4B-like myelin outfoldings [(18); Fig. 1]. Our study demonstrates that a null-type mutation in *Mtmr5* does not provoke CMT4B-like myelin outfoldings in mice. Therefore, we speculate that the M417V and T1590A mutations in *MTMR5* may trigger CMT in a manner distinct from that caused by *MTMR5* elimination (18). One possible mechanism for such an affect might be that mutations M417V and/or T1590A alter *MTMR5* in a manner that changes the pseudophosphatase's interaction with its binding partner *MTMR2*. If a mutated *MTMR5* protein were to impair *MTMR2* function, myelin outfoldings might be predicted to result.

***Mtmr5* and *Mtmr13* form distinct protein complexes with *Mtmr2* in the PNS**

Both *Mtmr5* and *Mtmr13* levels were enhanced when the proteins were expressed with their binding partner *Mtmr2*; this effect was observed both *in vitro* and in the PNS. We also observed that *Mtmr5* and *Mtmr13* are likely capable of associating in a manner that does not require *Mtmr2*. Notably, and unlike their associations with *Mtmr2*, interactions between *Mtmr5* and *Mtmr13* did not result in reciprocal enhancements of protein abundance. If extant, an *Mtmr5*–*Mtmr13* complex would be incapable of dephosphorylating PI3P or PI(3,5)P₂, key regulators of trafficking through early endosomes and lysosomes. Therefore, we hypothesize that two distinct myotubularin protein complexes form in the PNS: an *Mtmr2*–*Mtmr5* complex and an *Mtmr2*–*Mtmr13* complex. These two complexes would have similar capacity to regulate endosomal trafficking by activating Rab GTPases and dephosphorylating PIs. In tissues outside the PNS, the *Mtmr2*–*Mtmr5* and *Mtmr2*–*Mtmr13* complexes likely have overlapping or redundant functions,

as loss of both *Mtmr5* and *Mtmr13* caused perinatal lethality.

We show here that, despite their redundant role(s) during embryonic development, *Mtmr5* and *Mtmr13* play distinct biological roles in peripheral nerves. The differing expression patterns of these two homologous proteins during postnatal nerve development, and in adulthood, may at least partially explain the stark difference between the *Mtmr5*^{-/-} and *Mtmr13*^{-/-} nerve phenotypes. *Mtmr5* levels were high during axon radial sorting, and decreased sharply after P7. *Mtmr13* levels were also high at P7, but decreased less precipitously thereafter than did *Mtmr5* levels. *Mtmr2* protein levels in sciatic nerves peaked at P3–P7 and fell significantly thereafter. Notably, *Mtmr5* mRNA is expressed at levels significantly lower than both *Mtmr2* and *Mtmr13* mRNA in adult mouse Schwann cells (43). Thus, protein and mRNA expression data, when combined with evidence for a stable physical association between *Mtmr2* and *Mtmr5*, suggest that *Mtmr5* may play a limited role in mouse nerve development after the completion of radial sorting. Accordingly, we propose that *Mtmr2* and *Mtmr5* function together in immature Schwann cells to control which axons are sorted for myelination (Fig. 9). Once large axons form 1:1 relationships with Schwann cells, an *Mtmr2*–*Mtmr13* complex may function to ensure orderly myelin wrapping, and to maintain myelin homeostasis in adulthood. We speculate that *Mtmr2* may act to stabilize both *Mtmr5* and *Mtmr13* at several stages of nerve development, as the absence of this protein leads to decreases in both *Mtmr5* and *Mtmr13* levels in sciatic nerves. In summary, we demonstrate here that, in most tissues, either *Mtmr5* or *Mtmr13* is sufficient for normal cell function. In contrast, the PNS may require both proteins, perhaps because of temporal differences in *Mtmr5* and *Mtmr13* expression.

Control of endosome trafficking by *Mtmr5* and *Mtmr13* during axon sorting and myelination

A majority of the molecularly-defined forms of demyelinating CMT are caused by mutations in endosomal regulatory proteins (12). Schwann cells select large axons for myelination by integrating signals from ErbB2/3 tyrosine kinase receptors on their cell surfaces (50–52). Abnormal trafficking of the ErbB2/3 receptor complex in Schwann cells has been proposed as a common mechanism linking multiple demyelinating subtypes of CMT (16). Our previous work, and that of others has suggested that appropriate regulation of endosomal PI3P levels in Schwann cells is critical to controlling ErbB2/3 trafficking, and the associated downstream signaling (9,24). Specifically, the loss of *Mtmr2* has been shown to increase ErbB2/3 activation during initial myelination (24). As both *Mtmr5* and *Mtmr13* physically associate with *Mtmr2*, we speculate that loss of either pseudophosphatase may also lead to increased ErbB2/3 activation, likely by altering receptor trafficking through endosomes. Further investigations focused on *Mtmr5* and *Mtmr13* may serve to clarify

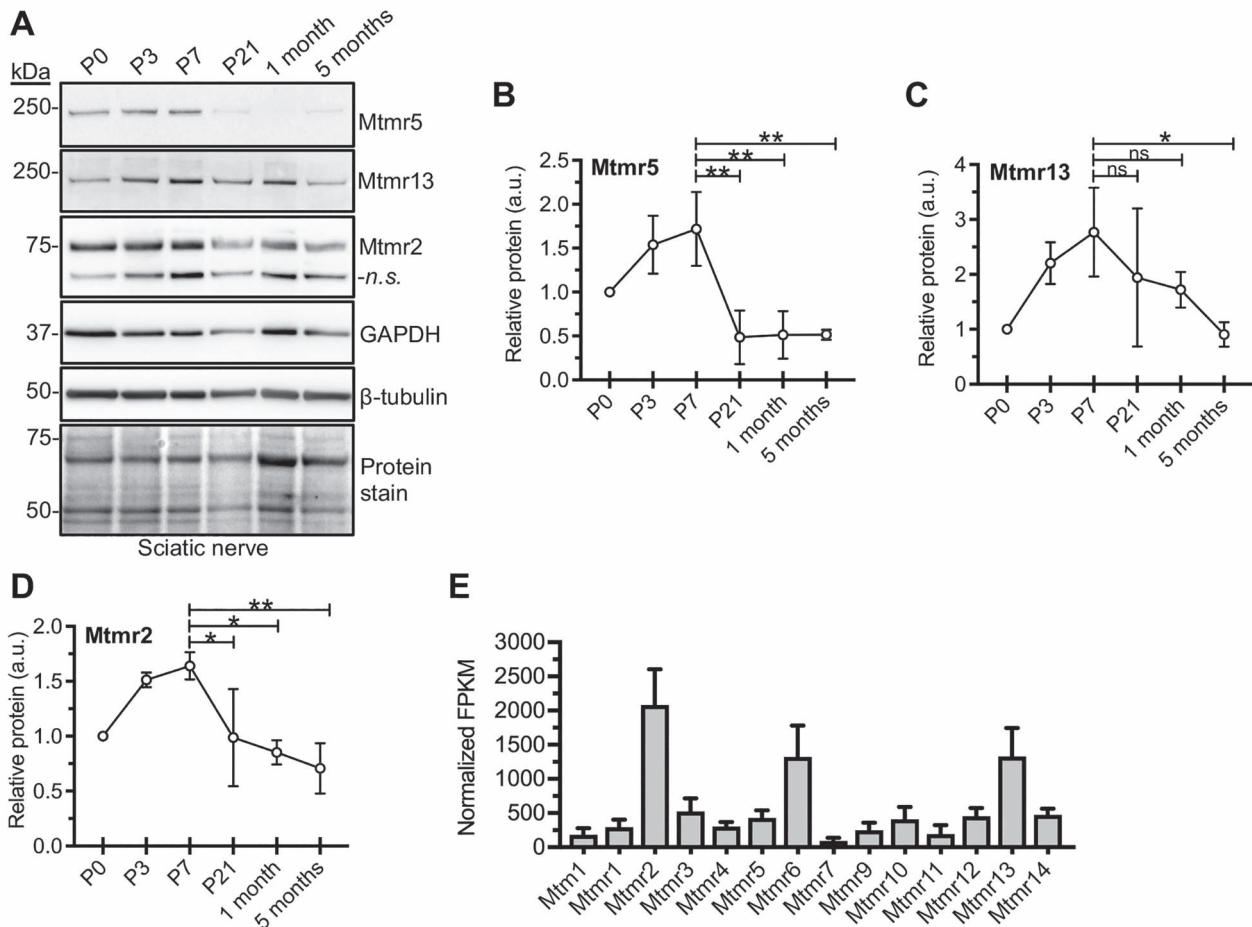


Figure 8. Myotubularin protein levels in mouse sciatic nerves and Schwann cells. **(A)** Immunoblot analysis of Mtmr5, Mtmr13 and Mtmr2 in wild-type mouse sciatic nerve extracts at P0, P3, P7, P21, 1 and 5 months. Representative immunoblots from one of three independent experiments are shown. A β -tubulin immunoblot and a total protein stain are shown as loading controls. **(B–D)** Relative protein abundance of Mtmr5, Mtmr13 and Mtmr2 at the indicated developmental stages. The levels of each protein at P3, P7, P21, 1 and 5 months are relative to the level of that protein at P0. Within each replicate immunoblot, the levels of Mtmr proteins were normalized to the GAPDH signal in the corresponding gel lane. Differences between protein levels at various time points were assessed with one-way ANOVA, followed by Sidak's multiple comparisons tests. Significant differences among the means were observed in the Mtmr2 and Mtmr5 ANOVA, ($P = 0.0006$ and 0.0025 , respectively), but not in the Mtmr13 ANOVA ($P = 0.0874$). For all three Mtmr proteins, significant decreases in abundance were observed after P7 (Sidak's multiple comparisons tests—Mtmr5: P7 vs. P21, $P = 0.0016^{**}$; P7 vs. 1 month, $P = 0.0019^{**}$; P7 vs. 5 months, $P = 0.0019^{**}$ —Mtmr13: P7 vs. P21, $P = 0.4595$ (n.s.); P7 vs. 1 month, $P = 0.2751$ (n.s.); P7 vs. 5 months, $P = 0.0280^{*}$ —Mtmr2: P7 vs. P21, $P = 0.0276^{*}$; P7 vs. 1 month, $P = 0.0102^{*}$; P7 vs. 5 months, $P = 0.0019^{**}$). Data points are mean \pm SD; $^{*}P \leq 0.05$; $^{**}P \leq 0.01$; $n = 3$ independent sciatic nerve extracts for all proteins at all time points except for Mtmr2 at the P21 and 1 month time points, where $n = 2$. **(E)** Relative mRNA expression of all 14 myotubularins in Schwann cells isolated from wild-type adult mouse sciatic nerves, presented as RNAseq-derived FPKM. The graph was generated using the publicly available Clements, M.P. et al. dataset (GSE103039) (43). Abbreviations: FPKM, Fragments Per Kilobase of transcript per Million mapped reads; ns, non-significant.

the dual role of ErbB2/3 in controlling axon sorting and myelination (53,54).

We speculate that Mtmr5 and Mtmr13 might also influence the trafficking of $\beta 1$ -integrin, which binds to laminin 211 in the Schwann cell basal lamina. The trafficking of $\beta 1$ -integrin through early endosomes is controlled by Rab21, which the DENN domain of Mtmr5/13 has been shown to activate (42). $\beta 1$ -integrin is required for the extension and maintenance of Schwann cell processes around axons; loss of this surface receptor leads to radial sorting defects and delayed myelination in mice (55). In *Mtmr5*^{-/-} nerves, we observed an increase in the proportion of unmyelinated axons that were incompletely ensheathed by Schwann cells. We speculate that this defect might be caused by a reduction in $\beta 1$ -integrin on the surface of *Mtmr5*^{-/-} Schwann cells, a result of

reduced recycling of the receptor from early endosomes. An analogous defect in $\beta 1$ -integrin trafficking has been demonstrated in *Mtmr5/13*-deficient *Drosophila* cells (42). Although ErbB2/3 and $\beta 1$ -integrin may presently be the best candidates for the signaling receptors influenced by Mtmr5/13-mediated endosomal trafficking, other yet to be identified surface proteins may also be regulated by these pseudophosphatases. For example, both tight junction proteins and G protein-coupled receptors are known to be regulated by endosomal trafficking (56,57). These two classes of proteins have been shown to regulate the Hippo-Yap signaling pathway, which translates extracellular signals, including mechanical tension, into changes in transcription (58). Yap and Taz, the terminal effectors of the pathway, play critical roles in the radial sorting of axons by Schwann cells (39,59).

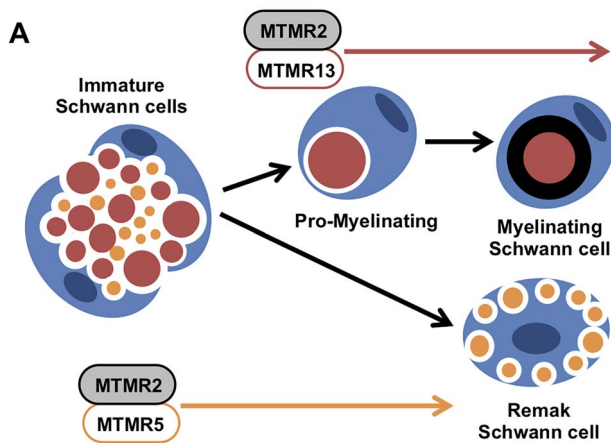


Figure 9. Proposed model for the respective roles of *Mtmr5* and *Mtmr13* in the PNS. We propose that two distinct myotubularin protein complexes form in the PNS: an *Mtmr2*–*Mtmr5* complex and an *Mtmr2*–*Mtmr13* complex. An *Mtmr2*–*Mtmr5* protein complex may positively regulate late stage axon radial sorting (E17–P10). Subsequently, an *Mtmr2*–*Mtmr13* protein complex may function to prevent abnormal myelin formations, once large axons have formed 1:1 relationships with promyelinating Schwann cells (P0 to adulthood). Differences in the timing of *Mtmr5* and *Mtmr13* expression may partially explain the impact of the loss of the two proteins on axon sorting and myelination, respectively.

Future investigations might therefore address whether abnormal trafficking of membrane proteins in the Hippo-Yap pathway contributes to the impaired radial sorting observed in *Mtmr5*^{−/−} nerves. Understanding how *Mtmr5* and *Mtmr13* regulate the trafficking of receptors involved in mediating axo-glia interactions and promyelinating signaling will likely be critical to discerning how the loss of these proteins leads to CMT.

In conclusion, we have shown, for the first time that *Mtmr5* positively regulates axon radial sorting in mouse peripheral nerves. This work demonstrates that *Mtmr5* plays a biological role distinct from that of the homologous *Mtmr13* protein, the loss of which causes demyelinating CMT4B2 in humans. Our study may inform investigations of those forms of CMT that result from loss-of-function mutations in *MTMR5*, and may aid in the definition of the cellular mechanisms that underpin this condition.

Materials and Methods

Mice

All animal work was approved by and conformed to the standards of the Oregon Health & Science University Animal Care and Use Committee. *Mtmr2*^{−/−} and *Mtmr13*^{−/−} mice have been previously described (22,33). An *Mtmr5* deletion allele was generated via CRISPR/Cas9 mutagenesis. To do so, two gRNAs were designed against exon 1 and exon 25 of the mouse *Mtmr5* gene using the online tool CRISPR Design. The following gRNAs were selected for their minimal off-target effects and potential to generate a large deletion beginning after the start-site (exon 1: GCTCGCGGACTACTTCGTGC) and ending after a putative internal initiation site (exon 25: CGTAAGAAGTATAACCCCC). These *Mtmr5*-specific

gRNA sequences were ligated into the *BbsI* restriction endonuclease site of px330 [addgene plasmid #42230; (60)]. Plasmids containing gRNAs plus Cas9 endonuclease were injected into the pronuclei of C57BL/6NJ mouse embryos. The embryo donors were oviduct transferred into CB6F1/J pseudopregnant recipient dams. *Mtmr5* founder mice were screened by PCR and Sanger sequencing to identify putative mutations in exon 1, exon 25, and large deletions between exon 1 and exon 25 using the following primers: forward exon 1 primer AMO-49 5′ CATGCGGAGTGGCCCAAT 3′, reverse exon 1 primer AMO-50 5′ GGATGTTTCTTACACAGGCCATGT 3′, forward exon 25 primer AMO-51 5′ CACGGGTTACCAAGGACAAG 3′, reverse exon 25 primer AMO-56 5′ GTCAACTCTGATAGC-GAGCACAG 3′. Mutations were confirmed by TOPO TA Thermo Fisher Scientific (Waltham, Massachusetts, U.S.A.) cloning and Sanger sequencing. Mice were bred to homozygosity and western blots were run to confirm *Mtmr5* protein loss in brain and sciatic nerve tissue. To test male sterility, six *Mtmr5*^{−/−} male mice were allowed to breed with C57BL/6 females for at least 21 days. Bred females were monitored for pregnancy and births for an additional three to four weeks.

Mtmr5^{−/−}; *Mtmr13*^{−/−} (dKO) mice were generated by crossing the *Mtmr5* CRISPR founder male with a *Mtmr13*^{−/−} female. *Mtmr5*^{+/−}; *Mtmr13*^{+/−} progeny were screened by PCR and Sanger sequencing for the *Mtmr5* large deletion using the following primers: AMO-49 5′ CATGCGGAGTGGCCCAAT 3′ and AMO-56 5′ GTCAACTCTGATAGCGAGCACAG 3′. The *Mtmr5*^{+/−}; *Mtmr13*^{+/−} mice were crossed with *Mtmr13*^{−/−} mice to generate *Mtmr5*^{+/−}; *Mtmr13*^{−/−} progeny. The *Mtmr5*^{+/−}; *Mtmr13*^{−/−} mice were interbred and their pups were genotyped at P0 to screen for dKO animals. Forty-nine pups from 13 litters were genotyped to assess the viability of *Mtmr5*^{−/−}; *Mtmr13*^{−/−} dKO mice.

Plasmid constructs

Mammalian expression vectors for human FLAG-MTMR2 (26), human EGFP-MTMR2 (61), human EGFP-MTMR13 and myc-MTMR13 mutant constructs (32) have been described. A human FLAG-MTMR5 expression vector (26) was modified to eliminate a single glutamine insertion between amino acid 93 and 94 and a K592M mutations. To generate the wild type construct human FLAG-MTMR5-AM1, transcript variant 1 from NM-002972.3 was amplified using oligonucleotides: 5′ GTT-TAAACTTAAAGCTTATGGCGCGGCTCGCGGAC 3′ and 5′ CCTGATGTCCGGCGGGTACCG 3′. The resulting PCR product was cloned into the previously described FLAG-MTMR5 construct, which had been digested with *KpnI* and *HindIII*, using In-Fusion Takara Bio (Kyoto, Japan).

Cell culture and immunoprecipitation

HEK293 cells were cultured in Dulbecco's Modified Eagle's Medium (DMEM; Gibco 11995-065), that was supplemented with 10% fetal bovine serum (FBS) and 1% penicillin/streptomycin. Cells were between 70 and

80% confluent at the time of transfection. A 60 mm dish was transfected with 2.5 μg of plasmid DNA, 7.5 μl X-tremeGENE9 Roche Applied Science (Penzberg, Upper Bavaria, Germany) and 250 μl of Opti-MEM Thermo Fisher Scientific (Waltham, Massachusetts, U.S.A.) according to manufacturer's instructions. Forty-eight hours after transfection, cells were washed with 1x phosphate-buffered saline (PBS) and lysed in 430 μl of ice-cold lysis buffer (120 mM NaCl, 50 mM Tris [pH 8.0], 0.5% Triton X-100, 100 mM NaF, 1 mM orthovanadate, 2 mM EDTA and a protease inhibitor cocktail [Roche 11836153001]). Lysates were vortexed and cleared by centrifugation (15 000 $\times g$ for 15 min at 4°C). Myc-tagged proteins were immunoprecipitated using anti-c-Myc monoclonal antibody supernatant (9E10, DSHB) and protein A-agarose Thermo Fisher Scientific (Waltham, Massachusetts, U.S.A.). Flag-tagged proteins were immunoprecipitated using anti-Flag-M2 affinity gel MilliporeSigma (Burlington, Massachusetts, U.S.A.). Immunoprecipitates were incubated for at least 2 h at 4°C, washed twice in 1 ml of lysis buffer, three times in 1 ml of lysis buffer containing 0.5 M NaCl, and once again in 1 ml of lysis buffer. Immunoprecipitates and lysates were suspended in 1x NuPAGE LDS sample buffer containing 10 mM DTT. Immunoprecipitates and lysates were resolved in 4–12% NuPAGE BisTris gels Thermo Fisher Scientific (Waltham, Massachusetts, U.S.A.) and transferred to polyvinylidene difluoride membranes for immunoblotting.

Immunoblotting

Immunoblotting of sciatic nerve, brain, HEK293 cell and MEF extracts was performed as previously described (22). Rabbit antibodies anti-MTMR13 (116-AN) and anti-MTMR2 (119-AN) have been described (22). Mouse anti-FLAG (M2) and anti-c-myc (9E10) were from MilliporeSigma (Burlington, Massachusetts, U.S.A.) and Roche Applied Science (Penzberg, Upper Bavaria, Germany), respectively. Mouse anti-Mtmt5 (B-9) was from Santa Cruz Biotechnology (Dallas, Texas, U.S.A.). Mouse anti-GFP antibody (N86/8) was from NeuroMab. Mouse anti- β tubulin (E7) and anti-GAPDH (MAB374) were from DSHB and MilliporeSigma (Burlington, Massachusetts, U.S.A.), respectively. For each P0, P3 and P7 lysate, nerves from three mice were pooled (6 nerves per lysate). For P21 and 1-month mouse extracts, nerves from two mice (4 nerves total) were pooled to generate each independent extract. Extracts from mice 3 months and older were generated from a single animal (2 nerves per lysate). For each immunoblot, 8–25 μm of protein per lane was resolved in 4–12% NuPAGE Bis-Tris gels Thermo Fisher Scientific (Waltham, Massachusetts, U.S.A.) and chemiluminescent quantitation was performed as previously described (23).

Sciatic nerve morphology

Mice were perfused with Karnovsky's EM fixative (4% paraformaldehyde, 2% glutaraldehyde; 0.1 M sodium cacodylate, pH 7.4). Sciatic nerves were dissected and

further fixed for at least 24 h at 4°C. Nerves were washed three times in 0.1 M sodium cacodylate (pH 7.4) and three times in 0.1 M sodium phosphate buffer (PB; pH 7.4) at room temperature (RT). Nerves were subsequently post-fixed and stained in 2% osmium tetroxide in 0.1 M PB buffer (pH 7.4) for 1 h. The nerves were then washed three times in 0.1 M PB at RT and underwent a series of ethanol dehydrations (25, 50, 70, 80 and 95%; 5 min each). A final dehydration was performed by incubating samples twice in 100% EtOH (10 min each), followed by two incubations in propylene oxide (10 min each). Nerves were infiltrated overnight in a 1:1 propylene oxide:Embed 812 resin mixture, and subsequently in freshly-prepared 100% Embed 812 resin. Nerves were embedded in a 60°C oven for 48 h. The distal end was positioned toward the beveled end of the mold to orient the nerves in the same direction. Ultra-thin (60 nm) sections were cut and subsequently arrayed on 400 mesh, thin-bar copper EM grids Electron Microscopy Sciences (Hatfield, Pennsylvania, U.S.A.).

Toluidine blue-stained semi-thin (200–500 μm) plastic cross-sections were prepared from the mid-sciatic nerve. Four non-overlapping images of nerve sections were acquired at 63x on a Zeiss Axio Imager M2 ApoTome microscope with an AxioCam 512 color camera. The tile feature in Zeiss Zen 2 (blue edition) software was used to capture the entire transverse fascicular area (TFA) of each nerve. To obtain total axon counts, tiled 63x Toluidine blue-stained images were used. All myelinated axons in the TFA were marked and counted using Cell Counter plugin for Fiji (62). G-ratio was determined using the G-ratio plugin for Fiji (63). Two hundred myelinated axons were randomly selected across 4 non-overlapping 63x Toluidine blue images of the TFA. To obtain an area-based G-ratio measurement, the area of the axon was divided by the area of the myelinated fiber. This measurement was then used to derive a diameter-based G-ratio measurement.

EM images were obtained using a FEI Tecnai G2 microscope operating at 80 kV and an Advanced Microscopy Techniques camera. To analyze Remak bundles, 2900x EM images were used. An axon bundle was defined as any group of two or more (unmyelinated) axons enwrapped by a Schwann cell. All intact Remak axons in the large fascicle of each nerve were analyzed. Each Remak axon was counted, and its area was measured. Any axon with an area $> 0.79 \mu\text{m}^2$ (1 μm in diameter) was considered large. 2900x EM images were also used to count abnormally ensheathed axons. At least 42% of the nerve TFA was exhaustively analyzed for each mouse.

Immunofluorescence

Whole-mount immunofluorescence of E13 mouse embryos with neurofilament medium chain (2H3) antibody was adapted from a published protocol (64). Individual embryos were stained in microcentrifuge tubes at RT, unless otherwise stated. Embryos were separated from placenta and amnion in 1x PBS, and 3 mm

of the tail was removed for use in genotyping. Embryos were fixed overnight at 4°C in 4% paraformaldehyde in 1x PBS solution (pH 7.4). After fixation, the embryos were washed with 1x PBS twice for 10 min. Embryos then underwent a series of methanol (MeOH) dehydrations (1 h in 50% MeOH in 1x PBS, 2 h 80% MeOH in 1x PBS, overnight in 100% MeOH). Embryos were bleached in 3% H₂O₂, 70% MeOH, 20% DMSO overnight and washed five times at 45 min intervals in 1x TNT (10 mM Tris, 154 mM NaCl, 0.1% Triton X-100). Bleached embryos were next incubated in a primary antibody solution (1x TNT, 0.02% sodium azide, 4% non-fat milk, 5% DMSO, 2% normal goat serum [NGS], 0.37 µg/ml 2H3 antibody) for 2–3 days. Embryos were washed five times in 1x TNT (45 min each), and subjected to a 2-day incubation in secondary antibody solution (1x TNT, 4% bovine serum albumin, 0.02% sodium azide, 5% DMSO, 2% NGS, 6.4 µg/ml Cy3 goat-anti-mouse (Jackson ImmunoResearch Laboratories (West Grove, Pennsylvania, U.S.A.), 115-175-205)). In all subsequent steps, the embryos were protected from light. Embryos are washed four times in 1x TBS (pH 7.4) for 45 min, then overnight in the same solution, and dehydrated using a MeOH series: 1 h in 50% MeOH (1x PBS), 2 h in 80% MeOH (1x PBS) and overnight in 100% MeOH. The samples were cleared in 1:2 BABB solution (Benzyl: Benzyl benzoate). Whole embryo images were taken on Zeiss AxioCam MR microscope at 1× magnification prior to the 1:2 BABB clearing step. Images of nerve branches were taken on a Zeiss ApoTome microscope at 5× magnification in 1:2 BABB solution.

Statistics

Statistical analyses of immunoblots, weight and morphology data were performed using a one-way ANOVA followed by post-hoc Tukey's or Sidak's multiple comparisons tests when more than two groups were compared. A Student's t-test was used when two groups were compared. A chi-squared (χ^2) test was performed to evaluate the significance of divergences from the expected frequencies of specific genotypes. The non-parametric Kolmogorov–Smirnov test (K–S test) was used for comparing the distribution of axon size. A probability value of ≤ 0.05 was used for assigning statistical significance. χ^2 and K–S tests were performed using R (version 3.5.1). The Prism software package (GraphPad) was used to perform ANOVA, Tukey multiple comparisons and Student's t-tests.

Supplementary Material

Supplementary Material is available at HMG online.

Acknowledgements

The authors wish to thank the OHSU Transgenic Mouse Models Shared Resource Core. The authors also wish to thank Matthew Pomaville and Kevin Wright for expert advice on mouse whole embryo immunofluorescence. The EM microscope was purchased through a Murdock

Charitable Trust grant to Sue Aicher. The authors would like to thank Ben Emery and Kelly Monk for constructive criticism and substantial feedback on the manuscript. The E7 (β -tubulin) monoclonal antibody was developed by Dr Michael Klymkowsky and obtained from Developmental Studies Hybridoma Bank (DSHB). The monoclonal antibody 2H3 (NF-M), developed by Drs T.M. Jessell and J. Dodd, was obtained from the DSHB developed under the National Institutes of Health-National Institute of Child Health & Human Development and maintained by The University of Iowa, Department of Biology, Iowa City, IA 52242. The authors also wish to acknowledge the philanthropy of Frank and Julie Jungers.

Conflict of Interest statement. The authors declare that they have no conflicts of interest.

Funding

National Institutes of Health-National Institute of Neurological Disorders and Stroke (grant NS086812 to F.L.R.); Oregon Health & Science University Neuroscience Imaging Center (grant NS061800; to S.A.A).

References

1. Feltri, M.L., Poitelon, Y. and Previtali, S.C. (2016) How Schwann cells sort axons: new concepts. *Neuroscientist*, **22**, 252–265.
2. Harty, B.L. and Monk, K.R. (2017) Unwrapping the unappreciated: recent progress in Remak Schwann cell biology. *Curr. Opin. Neurobiol.*, **47**, 131–137.
3. Salzer, J.L. (2015) Schwann cell myelination. *Cold Spring Harb. Perspect. Biol.*, **7**, a020529.
4. Rasband, M.N. and Peles, E. (2015) The nodes of Ranvier: molecular assembly and maintenance. *Cold Spring Harb. Perspect. Biol.*, **8**, a020495.
5. Kleopa, K.A. and Sargiannidou, I. (2015) Connexins, gap junctions and peripheral neuropathy. *Neurosci. Lett.*, **596**, 27–32.
6. Beirowski, B. (2019) The LKB1-AMPK and mTORC1 metabolic signaling networks in Schwann cells control axon integrity and myelination: assembling and upholding nerves by metabolic signaling in Schwann cells. *BioEssays*, **41**, e1800075.
7. Pooya, S., Liu, X., Kumar, V.B., Anderson, J., Imai, F., Zhang, W., Ciraolo, G., Ratner, N., Setchell, K.D., Yoshida, Y. et al. (2014) The tumour suppressor LKB1 regulates myelination through mitochondrial metabolism. *Nat. Commun.*, **5**, 4993.
8. Viader, A., Golden, J.P., Baloh, R.H., Schmidt, R.E., Hunter, D.A. and Milbrandt, J. (2011) Schwann cell mitochondrial metabolism supports long-term axonal survival and peripheral nerve function. *J. Neurosci.*, **31**, 10128–10140.
9. Logan, A.M., Mammel, A.E., Robinson, D.C., Chin, A.L., Condon, A.F. and Robinson, F.L. (2017) Schwann cell-specific deletion of the endosomal PI 3-kinase Vps34 leads to delayed radial sorting of axons, arrested myelination, and abnormal ErbB2-ErbB3 tyrosine kinase signaling. *Glia*, **65**, 1452–1470.
10. Gouttenoire, E.A., Lupo, V., Calpena, E., Bartesaghi, L., Schupfer, F., Medard, J.J., Maurer, F., Beckmann, J.S., Senderek, J., Palau, F. et al. (2013) Sh3tc2 deficiency affects neuregulin-1/ErbB signaling. *Glia*, **61**, 1041–1051.
11. Sidiropoulos, P.N., Miehe, M., Bock, T., Tinelli, E., Oertli, C.I., Kuner, R., Meijer, D., Wollscheid, B., Niemann, A. and Suter, U.

- (2012) Dynamin 2 mutations in Charcot-Marie-Tooth neuropathy highlight the importance of clathrin-mediated endocytosis in myelination. *Brain*, **135**, 1395–1411.
12. Brennan, K.M., Bai, Y. and Shy, M.E. (2015) Demyelinating CMT—what's known, what's new and what's in store. *Neurosci. Lett.*, **596**, 14–26.
 13. Jerath, N.U. and Shy, M.E. (2015) Hereditary motor and sensory neuropathies: understanding molecular pathogenesis could lead to future treatment strategies. *Biochim. Biophys. Acta*, **1852**, 667–678.
 14. Shy, M.E. (2011) Inherited peripheral neuropathies. *Continuum (Minneapolis)*, **17**, 294–315.
 15. Bird, T.D. (1993) In Adam, M.P., Ardinger, H.H., Pagon, R.A., Wallace, S.E., Bean, L.J.H., Stephens, K. and Amemiya, A. (eds), *GeneReviews*(®). Press, Seattle (WA).
 16. Lee, S.M., Chin, L.S. and Li, L. (2017) Dysregulation of ErbB receptor trafficking and signaling in demyelinating Charcot-Marie-Tooth disease. *Mol. Neurobiol.*, **54**, 87–100.
 17. Bolino, A., Muglia, M., Conforti, F.L., LeGuern, E., Salih, M.A., Georgiou, D.M., Christodoulou, K., Hausmanowa-Petrusewicz, I., Mandich, P., Schenone, A. et al. (2000) Charcot-Marie-Tooth type 4B is caused by mutations in the gene encoding myotubularin-related protein-2. *Nat. Genet.*, **25**, 17–19.
 18. Nakhro, K., Park, J.M., Hong, Y.B., Park, J.H., Nam, S.H., Yoon, B.R., Yoo, J.H., Koo, H., Jung, S.C., Kim, H.L. et al. (2013) SET binding factor 1 (SBF1) mutation causes Charcot-Marie-Tooth disease type 4B3. *Neurology*, **81**, 165–173.
 19. Senderek, J., Bergmann, C., Weber, S., Ketelsen, U.P., Schorle, H., Rudnik-Schoneborn, S., Buttner, R., Buchheim, E. and Zerres, K. (2003) Mutation of the SBF2 gene, encoding a novel member of the myotubularin family, in Charcot-Marie-Tooth neuropathy type 4B2/11p15. *Hum. Mol. Genet.*, **12**, 349–356.
 20. Amoasii, L., Hnia, K. and Laporte, J. (2012) Myotubularin phosphoinositide phosphatases in human diseases. *Curr. Top. Microbiol. Immunol.*, **362**, 209–233.
 21. Taylor, G.S., Maehama, T. and Dixon, J.E. (2000) Myotubularin, a protein tyrosine phosphatase mutated in myotubular myopathy, dephosphorylates the lipid second messenger, phosphatidylinositol 3-phosphate. *Proc. Natl. Acad. Sci. U. S. A.*, **97**, 8910–8915.
 22. Ng, A.A., Logan, A.M., Schmidt, E.J. and Robinson, F.L. (2013) The CMT4B disease-causing phosphatases Mtmr2 and Mtmr13 localize to the Schwann cell cytoplasm and endomembrane compartments, where they depend upon each other to achieve wild-type levels of protein expression. *Hum. Mol. Genet.*, **22**, 1493–1506.
 23. Robinson, D.C., Mammel, A.E., Logan, A.M., Larson, A.A., Schmidt, E.J., Condon, A.F. and Robinson, F.L. (2018) An in vitro model of Charcot-Marie-Tooth disease type 4B2 provides insight into the roles of MTMR13 and MTMR2 in Schwann cell myelination. *ASN Neuro*, **10**, 1759091418803282.
 24. Bolino, A., Piguat, F., Alberizzi, V., Pellegatta, M., Rivellini, C., Guerrero-Valero, M., Nosedà, R., Brombin, C., Nonis, A., D'Adamo, P. et al. (2016) Niacin-mediated Tace activation ameliorates CMT neuropathies with focal hypermyelination. *EMBO Mol Med*, **8**, 1438–1454.
 25. Vaccari, I., Dina, G., Tronchere, H., Kaufman, E., Chicanne, G., Cerri, F., Wrabetz, L., Payrastre, B., Quattrini, A., Weisman, L.S. et al. (2011) Genetic interaction between MTMR2 and FIG 4 phospholipid phosphatases involved in Charcot-Marie-Tooth neuropathies. *PLoS Genet.*, **7**, e1002319.
 26. Kim, S.A., Vacratsis, P.O., Firestein, R., Cleary, M.L. and Dixon, J.E. (2003) Regulation of myotubularin-related (MTMR)2 phosphatidylinositol phosphatase by MTMR5, a catalytically inactive phosphatase. *Proc. Natl. Acad. Sci. U. S. A.*, **100**, 4492–4497.
 27. Flusser, H., Halperin, D., Kadir, R., Shorer, Z., Shelef, I. and Birk, O.S. (2018) Novel SBF1 splice-site null mutation broadens the clinical spectrum of Charcot-Marie-Tooth type 4B3 disease. *Clin. Genet.*, **94**, 473–479.
 28. Manole, A., Horga, A., Gamez, J., Raguer, N., Salvado, M., San Millan, B., Navarro, C., Pittmann, A., Reilly, M.M. and Houlden, H. (2017) SBF1 mutations associated with autosomal recessive axonal neuropathy with cranial nerve involvement. *Neurogenetics*, **18**, 63–67.
 29. Alazami, A.M., Alzahrani, F., Bohlega, S. and Alkuraya, F.S. (2014) SET binding factor 1 (SBF1) mutation causes Charcot-Marie-tooth disease type 4B3. *Neurology*, **82**, 1665–1666.
 30. Romani, M., Mehawej, C., Mazza, T., Megarbane, A. and Valente, E.M. (2016) "Fork and bracket" syndrome expands the spectrum of SBF1-related sensory motor polyneuropathies. *Neurol Genet*, **2**, e61.
 31. Firestein, R., Nagy, P.L., Daly, M., Huie, P., Conti, M. and Cleary, M.L. (2002) Male infertility, impaired spermatogenesis, and azoospermia in mice deficient for the pseudophosphatase Sbf1. *J. Clin. Invest.*, **109**, 1165–1172.
 32. Robinson, F.L. and Dixon, J.E. (2005) The phosphoinositide-3-phosphatase MTMR2 associates with MTMR13, a membrane-associated pseudophosphatase also mutated in type 4B Charcot-Marie-Tooth disease. *J. Biol. Chem.*, **280**, 31699–31707.
 33. Robinson, F.L., Niesman, I.R., Beiswenger, K.K. and Dixon, J.E. (2008) Loss of the inactive myotubularin-related phosphatase Mtmr13 leads to a Charcot-Marie-Tooth 4B2-like peripheral neuropathy in mice. *Proc. Natl. Acad. Sci. U. S. A.*, **105**, 4916–4921.
 34. Tersar, K., Boentert, M., Berger, P., Bonneick, S., Wessig, C., Toyka, K.V., Young, P. and Suter, U. (2007) Mtmr13/Sbf2-deficient mice: an animal model for CMT4B2. *Hum. Mol. Genet.*, **16**, 2991–3001.
 35. Azzedine, H., Bolino, A., Taieb, T., Birouk, N., Di Duca, M., Bouhouche, A., Benamou, S., Mrabet, A., Hammadouche, T., Chkili, T. et al. (2003) Mutations in MTMR13, a new pseudophosphatase homologue of MTMR2 and Sbf1, in two families with an autosomal recessive demyelinating form of Charcot-Marie-Tooth disease associated with early-onset glaucoma. *Am. J. Hum. Genet.*, **72**, 1141–1153.
 36. Lancaster, E., Li, J., Hanania, T., Liem, R., Scheideler, M.A. and Scherer, S.S. (2018) Myelinated axons fail to develop properly in a genetically authentic mouse model of Charcot-Marie-tooth disease type 2E. *Exp. Neurol.*, **308**, 13–25.
 37. Kudryashova, E., Wu, J., Havton, L.A. and Spencer, M.J. (2009) Deficiency of the E3 ubiquitin ligase TRIM32 in mice leads to a myopathy with a neurogenic component. *Hum. Mol. Genet.*, **18**, 1353–1367.
 38. Poitelon, Y., Bogni, S., Matafora, V., Della-Flora Nunes, G., Hurley, E., Ghidinelli, M., Katzenellenbogen, B.S., Taveggia, C., Silvestri, N., Bachi, A. et al. (2015) Spatial mapping of juxtacrine axo-glial interactions identifies novel molecules in peripheral myelination. *Nat. Commun.*, **6**, 8303.
 39. Poitelon, Y., Lopez-Anido, C., Catignas, K., Berti, C., Palmisano, M., Williamson, C., Ameroso, D., Abiko, K., Hwang, Y., Gregorieff, A. et al. (2016) YAP and TAZ control peripheral myelination and the expression of laminin receptors in Schwann cells. *Nat. Neurosci.*, **19**, 879–887.
 40. Robinson, F.L. and Dixon, J.E. (2006) Myotubularin phosphatases: policing 3-phosphoinositides. *Trends Cell Biol.*, **16**, 403–412.
 41. Burgo, A., Sotirakis, E., Simmler, M.C., Verraes, A., Chamot, C., Simpson, J.C., Lanzetti, L., Proux-Gillardeaux, V. and Galli,

- T. (2009) Role of Varp, a Rab21 exchange factor and TI-VAMP/VAMP7 partner, in neurite growth. *EMBO Rep.*, **10**, 1117–1124.
42. Jean, S., Cox, S., Schmidt, E.J., Robinson, F.L. and Kiger, A. (2012) Sbf/MTMR13 coordinates PI(3)P and Rab21 regulation in endocytic control of cellular remodeling. *Mol. Biol. Cell*, **23**, 2723–2740.
 43. Clements, M.P., Byrne, E., Camarillo Guerrero, L.F., Cattin, A.L., Zakka, L., Ashraf, A., Burden, J.J., Khadayate, S., Lloyd, A.C., Marguerat, S. et al. (2017) The wound microenvironment reprograms Schwann cells to invasive mesenchymal-like cells to drive peripheral nerve regeneration. *Neuron*, **96**, 98, e117–114.
 44. Auer-Grumbach, M., Toegel, S., Schabhuettel, M., Weinmann, D., Chiari, C., Bennett, D.L.H., Beetz, C., Klein, D., Andersen, P.M., Bohme, I. et al. (2016) Rare variants in MME, encoding metalloprotease Nephrilysin, are linked to late-onset autosomal-dominant axonal polyneuropathies. *Am. J. Hum. Genet.*, **99**, 607–623.
 45. Balastik, M., Ferraguti, F., Pires-da Silva, A., Lee, T.H., Alvarez-Bolado, G., Lu, K.P. and Gruss, P. (2008) Deficiency in ubiquitin ligase TRIM2 causes accumulation of neurofilament light chain and neurodegeneration. *Proc. Natl. Acad. Sci. U. S. A.*, **105**, 12016–12021.
 46. Barneo-Munoz, M., Juarez, P., Civera-Tregon, A., Yndriago, L., Pla-Martin, D., Zenker, J., Cuevas-Martin, C., Estela, A., Sanchez-Arago, M., Forteza-Vila, J. et al. (2015) Lack of GDAP1 induces neuronal calcium and mitochondrial defects in a knockout mouse model of charcot-marie-tooth neuropathy. *PLoS Genet.*, **11**, e1005115.
 47. Strickland, A.V., Rebelo, A.P., Zhang, F., Price, J., Bolon, B., Silva, J.P., Wen, R. and Zuchner, S. (2014) Characterization of the mitofusin 2 R94W mutation in a knock-in mouse model. *J. Peripher. Nerv. Syst.*, **19**, 152–164.
 48. Zhu, Q., Lindenbaum, M., Levavasseur, F., Jacomy, H. and Julien, J.P. (1998) Disruption of the NF-H gene increases axonal microtubule content and velocity of neurofilament transport: relief of axonopathy resulting from the toxin beta,beta'-iminodipropionitrile. *J. Cell Biol.*, **143**, 183–193.
 49. Taveggia, C., Zanazzi, G., Petrylak, A., Yano, H., Rosenbluth, J., Einheber, S., Xu, X., Esper, R.M., Loeb, J.A., Shrager, P. et al. (2005) Neuregulin-1 type III determines the ensheathment fate of axons. *Neuron*, **47**, 681–694.
 50. Salzer, J.L. (2012) Axonal regulation of Schwann cell ensheathment and myelination. *J. Peripher. Nerv. Syst.*, **17**(Suppl 3), 14–19.
 51. Nave, K.A. and Salzer, J.L. (2006) Axonal regulation of myelination by neuregulin 1. *Curr. Opin. Neurobiol.*, **16**, 492–500.
 52. Birchmeier, C. and Bennett, D.L. (2016) Neuregulin/ErbB signaling in developmental myelin formation and nerve repair. *Curr. Top. Dev. Biol.*, **116**, 45–64.
 53. Garratt, A.N., Voiculescu, O., Topilko, P., Charnay, P. and Birchmeier, C. (2000) A dual role of erbB2 in myelination and in expansion of the schwann cell precursor pool. *J. Cell Biol.*, **148**, 1035–1046.
 54. Raphael, A.R., Lyons, D.A. and Talbot, W.S. (2011) ErbB signaling has a role in radial sorting independent of Schwann cell number. *Glia*, **59**, 1047–1055.
 55. Feltri, M.L., Graus Porta, D., Previtali, S.C., Nodari, A., Migliavacca, B., Casseti, A., Littlewood-Evans, A., Reichardt, L.F., Messing, A., Quattrini, A. et al. (2002) Conditional disruption of beta 1 integrin in Schwann cells impedes interactions with axons. *J. Cell Biol.*, **156**, 199–209.
 56. Stamatovic, S.M., Johnson, A.M., Sladojevic, N., Keep, R.F. and Andjelkovic, A.V. (2017) Endocytosis of tight junction proteins and the regulation of degradation and recycling. *Ann. N. Y. Acad. Sci.*, **1397**, 54–65.
 57. Weinberg, Z.Y. and Puthenveedu, M.A. (2019) Regulation of G protein-coupled receptor signaling by plasma membrane organization and endocytosis. *Traffic*, **20**, 121–129.
 58. Meng, Z., Moroishi, T. and Guan, K.L. (2016) Mechanisms of Hippo pathway regulation. *Genes Dev.*, **30**, 1–17.
 59. Deng, Y., Wu, L.M.N., Bai, S., Zhao, C., Wang, H., Wang, J., Xu, L., Sakabe, M., Zhou, W., Xin, M. et al. (2017) A reciprocal regulatory loop between TAZ/YAP and G-protein Galphas regulates Schwann cell proliferation and myelination. *Nat. Commun.*, **8**, 15161.
 60. Cong, L., Ran, F.A., Cox, D., Lin, S., Barretto, R., Habib, N., Hsu, P.D., Wu, X., Jiang, W., Marraffini, L.A. et al. (2013) Multiplex genome engineering using CRISPR/Cas systems. *Science*, **339**, 819–823.
 61. Kim, S.A., Taylor, G.S., Torgersen, K.M. and Dixon, J.E. (2002) Myotubularin and MTMR2, phosphatidylinositol 3-phosphatases mutated in myotubular myopathy and type 4B Charcot-Marie-Tooth disease. *J. Biol. Chem.*, **277**, 4526–4531.
 62. Schindelin, J., Arganda-Carreras, I., Frise, E., Kaynig, V., Longair, M., Pietzsch, T., Preibisch, S., Rueden, C., Saalfeld, S., Schmid, B. et al. (2012) Fiji: an open-source platform for biological-image analysis. *Nat. Methods*, **9**, 676–682.
 63. Goebbels, S., Oltrogge, J.H., Kemper, R., Heilmann, I., Bormuth, I., Wolfer, S., Wichert, S.P., Mobius, W., Liu, X., Lappe-Siefke, C. et al. (2010) Elevated phosphatidylinositol 3,4,5-trisphosphate in glia triggers cell-autonomous membrane wrapping and myelination. *J. Neurosci.*, **30**, 8953–8964.
 64. Merte, J., Wang, Q., Vander Kooi, C.W., Sarsfield, S., Leahy, D.J., Kolodkin, A.L. and Ginty, D.D. (2010) A forward genetic screen in mice identifies Sema3A(K108N), which binds to neuropilin-1 but cannot signal. *J. Neurosci.*, **30**, 5767–5775.